Ceramics International 44 (2018) 10393–10401

Contents lists available at ScienceDirect

Ceramics International

journal homepage: www.elsevier.com/locate/ceramint

Influence of ionic liquid on the photoelectrochemical properties of ZnO particles

Letícia G. da Trindade[a,*], Gabriela B. Minervino[b], Aline B. Trench[a], Maria H. Carvalho[c], Marcelo Assis[a], Máximo S. Li[d], Adilson J.A. de Oliveira[c], Ernesto C. Pereira[a], Tatiana M. Mazzo[b], Elson Longo[a]

[a] Chemistry Department – CDMF/LIEC, UFSCar, P.O. Box 676, 13565-905 São Carlos, SP, Brazil
[b] Institute of Marine Sciences-Federal University of São Paulo (UNIFESP), P.O. Box 11070-100, Santos, SP, Brazil
[c] Physics Department, UFSCar, P.O. Box 676, 13565-905 São Carlos, SP, Brazil
[d] IFSC, Universidade de São Paulo, P.O. Box 369, 13569-970 São Carlos, SP, Brazil

ARTICLE INFO

Keywords:
(C) Optical properties
(D) ZnO
(E) Electrodes

ABSTRACT

ZnO particles synthesized by the microwave-assisted hydrothermal method were sensitized with different amounts of ionic liquid (IL) 1.3-dimethylimidazolium iodide (MMI.I). The structure of the modified and unmodified ZnO particles were characterized by X-ray diffraction, Raman spectroscopy, field emission gun-scanning electron microscopy (FEG-SEM), ultraviolet-visible (UV–vis) absorption spectroscopy, photoluminescence (PL), and photoelectrochemical measurements. While the sensitization of ZnO particles by the ionic liquid does not change the ZnO phase, it reduces the particle size and converts shallow defects to deep defects. These changes cause the photocurrent density of the ZnO/IL films to increase significantly from 0.05 mA cm^{-2} for pure ZnO to 0.52 and 1.24 mA cm^{-2} for the ZnO films containing 20% and 35% by mass of the IL, respectively, at 1.08 V vs. Ag/AgCl. This about 24-fold increase in the photocurrent density of the ZnO/IL35 sample may indicate that the MMI.I IL may be acting as a dye, since it is constituted by an organic part, MMI^{+}. This good performance presented by this sample indicates that this is a promising material for photoanode in solar cells.

1. Introduction

The environmental impact of the use of fossil fuels has motivated the research into alternative energy sources. Renewable energies, such as biofuels [1], fuel cells [2], and solar cells [3], have emerged as possible solutions to overcome this problem. Among the renewable energy sources, solar energy must be considered because it is an inexhaustible source of both heat and light. Among the electrochemical energy conversion devices, dye-sensitized solar cells (DSSCs) are a promising alternative once they are simple to manufacture, inexpensive, eco-friendly, and display high-energy conversion efficiency [3]. Generally, DSSCs have photoanodes fabricated with n-type semiconducting oxides, such as TiO_2, ZnO, and SnO_2 [4–6]. In recent years, ZnO with modulated nanostructured morphology has been intensively investigated, because its band gap (3.37 eV) [7] is comparable to that of TiO_2, while presenting higher electron mobility (2–3 orders of magnitude higher) [8] leading to fast electron transport and consequently reduced recombination loss [9].

Ionic liquids (ILs) are room temperature molten salts that consist of aromatic or non-aromatic organic cations that can be combined with anions. ILs exhibit high chemical and thermal stability, non-volatility, non-flammability, high ionic conductivity, and a wide electrochemical window [10,11]. Due to these characteristics, they are proposed to improve properties in different fields such as non-volatile organic green solvents [12], environmentally benign separation processes [13], batteries [14], fuel cells [15], supercapacitors [16], and DSSCs [17]. ILs based on imidazolium cations have been widely used as electrolyte solvents for DSSCs. However, they have high viscosity as a major drawback, resulting in small diffusion coefficients of the redox-couple [18]. An alternative method to overcome this disadvantage is to introduce the IL into a polymer electrolyte.

Latip et al. [19] prepared ionic liquid polymer electrolytes (ILPE) with poly(1-vinylpyrrolidone-*co*-vinylacetate), P(VP-*co*-VAc), copolymer, tetrahexylammonium iodide (THAI) salt, and 1-butyl-3-methylimidazolium iodide (BMI.I). The highest ionic conductivity obtained in this system, at room temperature, has been 1.05 mS cm^{-1}, which was the sample incorporated with 80 wt% of BMI.I. In addition, a DSSC built using this electrolyte displayed a maximum power conversion

* Corresponding author.
E-mail address: leticiagt@terra.com.br (L.G. da Trindade).

https://doi.org/10.1016/j.ceramint.2018.03.053
Received 18 December 2017; Received in revised form 27 February 2018; Accepted 7 March 2018
Available online 08 March 2018
0272-8842/ © 2018 Elsevier Ltd and Techna Group S.r.l. All rights reserved.

efficiency (h) of 4.93% along with a short circuit current density (J_{sc}), open circuit voltage (V_{oc}), and fill factor (FF) of 12.37 mA cm^{-2}, 0.69 V, and 0.58, respectively.

It is important to stress out that the properties of ionic liquids can be tuned by controlling the structure of cations and anions. From a different point of view, the mechanism of the observer effects on the performance of modified materials for use in DSSCs has not yet been fully clarified. Considering these aspects, we report herein the preparation and characterization of ZnO particles with the 1.3-dimethylimidazolium iodide (MMI.I) IL incorporated into the oxide in two different proportions for possible solar cell photoanodes application.

2. Material and methods

2.1. Synthesis

ZnO particles were prepared by the microwave assisted hydrothermal method. Zinc nitrate (0.03 mol L^{-1}) was dissolved in 50 ml of deionized water under constant stirring, followed by the addition of 50 ml of KOH solution (2.0 mol L^{-1}). This solution was transferred to a reactor and heated in a Panasonic® modified microwave oven (Model MN-S46B), at a frequency of 2450 MHz and power of 1050 W. The reactor was heated to 140 °C, and this temperature was maintained for 32 min followed by cooling. The reaction products were washed with deionized water at pH 7 and then oven-dried for 12 h at 60 °C.

The synthesis of 1.3-dimethylimidazolium iodide ionic liquid was carried out by the procedure described in the literature [20].

2.2. Electrode preparation

Viscous pastes of ZnO, ZnO/IL20, and ZnO/IL35 were prepared by mixing 0.0125 g of ZnO with 200 µL of ethanol, or 0.0125 g of ZnO with 20% or 35% by mass of MMI.I IL in 200 µL of ethanol. This mixture was sonicated for 30 min, followed by the addition of 60 µL of deionized water and sonication for another 30 min. The obtained suspensions were applied onto fluorine-doped tin oxide (FTO) substrates of area 1 cm^2, using a micropipette. The films were then allowed to dry in air for 1 h, and then calcined at 400 °C for 1 h, at heating and cooling rates of 0.5 °C min^{-1}, in order to avoid cracking of the film.

2.3. Material characterization

The films were investigated by X-ray diffraction (XRD), Attenuated total reflectance Fourier transform infrared spectroscopy (ATR-FTIR), Raman spectroscopy, thermogravimetric analysis (TGA), field emission gun-scanning electron microscopy (FEG-SEM), ultraviolet-visible (UV–vis) absorption spectroscopy, photoluminescence (PL) spectroscopy, and photoelectrochemical methods.

XRD patterns were recorded using a Shimadzu XRD 6000 diffractometer, with Cu Kα radiation (λ = 0.15406 nm), in the 2θ range 5–120° with 0.02° min^{-1} increments. Rietveld analysis [21] was performed using the GSAS-EXPGUI software [22,23]. ATR-FTIR spectra with a Bruker Alpha-P spectrometer in the scanning range 4000–400 cm^{-1}. Raman spectra were recorded at room temperature using a triple grating JobinYvon T64000 spectrometer equipped with a liquid nitrogen cooled charge coupled device (CCD). The Raman instrument was coupled to a standard Olympus microscope and a collection optics system. The excitation source was a 514.5 nm Ar+ laser line. The optical power at the sample position was maintained at 5 mW. The scattered light was collected in the backscattering configuration and the spectra were recorded at a resolution of 2.0 cm^{-1}. Thermogravimetric analysis (TGA) was performed under nitrogen (N_2) atmosphere (TA Instruments Q-50 apparatus) in the temperature range 25–850 °C at a heating rate of 10 °C min^{-1}. The surface morphology was studied by FEG-SEM using a ZEISS model 105 DSM940A instrument working at 10 keV. UV–vis absorption spectra were recorded in the total diffuse reflectance mode on a Cary 5 G (Varian, USA) equipment. PL measurements were obtained in the 350–850 nm range with a Thermal Jarrel-Ash Monospec 27 cm monochromator and a Hamamatsu R955 Photomultiplier. The 350.7 nm (2.57 eV) exciting wavelength of a krypton ion laser (Coherent Innova 200) was used and the output of the laser was maintained at 500 mW, arriving 14 mW on the sample.

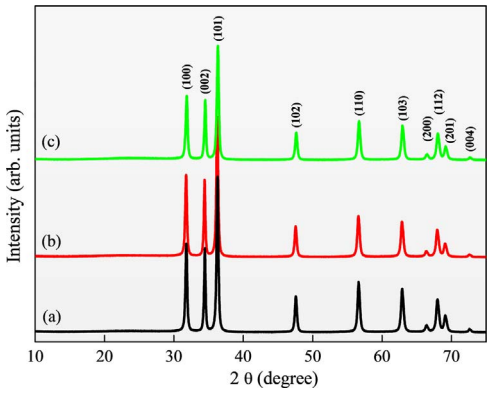

Fig. 1. XRD patterns of ZnO (a), ZnO/IL20 (b), and ZnO/IL35 (c) samples.

Photoelectrochemical measurements were carried out in a quartz glass cell, using an Autolab PGSTAT 302 N instrument, with the three-electrode configuration composed of the as-prepared samples as working electrode, Pt foil as counter electrode, and a saturated Ag/AgCl reference electrode dipped in an acetonitrile solution with 10 mM LiI, 1 mM I_2, and 0.1 M $LiClO_4$. The light source was simulated sunlight from a 100 W Xenon solar simulator Newport Sol3A ClassAAA. Current density–voltage (J–V) curves were measured under light and dark with a scanning rate of 20 mV s^{-1}, between 0.8 and 1.6 V.

3. Results and discussion

The polycrystalline nature of the ZnO and sensitized ZnO samples was evaluated by the XRD patterns and Rietveld refinement analysis. Fig. 1 shows the XRD patterns of pure and modified ZnO samples.

All the XRD patterns correspond to the hexagonal wurtzite structure and are in agreement with the Inorganic Crystal Structure Database card (ICSD card No. 57450) for the pure ZnO phase with space group *P*63*mc*. It can be seen that the addition of ionic liquid do not alter the crystal phase of ZnO. The obtained values for lattice parameters, unit cell volume, mean crystallite size, isotropic strain, R weighted (R_{WP}), and goodness of fit (S) are presented in Table 1. The statistical values obtained indicate a good quality refinement and are in agreement with the literature reports [24,25]. From the results, we can observe that insertion of the IL did not significantly change the lattice parameters of ZnO. However, a decrease in the average size of the crystallite can be observed with increasing IL concentration.

ATR-FTIR analyses were performed to study the possible interaction between MMI.I IL and ZnO particles. Fig. 2(A) shows the ATR-FTIR spectra of the samples in the 4000–480 cm^{-1} range. This figure shows that the ZnO particles shows bands at 480–590 cm^{-1} that are attributed

Table 1
Rietveld refinement results of the pure and sensitized ZnO samples.

Sample	Lattice Parameter (Å)		Cell volume V (Å^3)	$< D_{X\text{-}ray} >$ (nm)	Strain (%)	R_{WP} (%)	S
	a = *b* (Å)	*c* (Å)					
ZnO	3.25	5.21	47.68	76.6	0.467	4.24	1.69
ZnO/IL20	3.25	5.21	47.68	69.0	0.472	4.81	1.98
ZnO/IL35	3.25	5.21	47.67	66.2	0.476	5.10	1.98

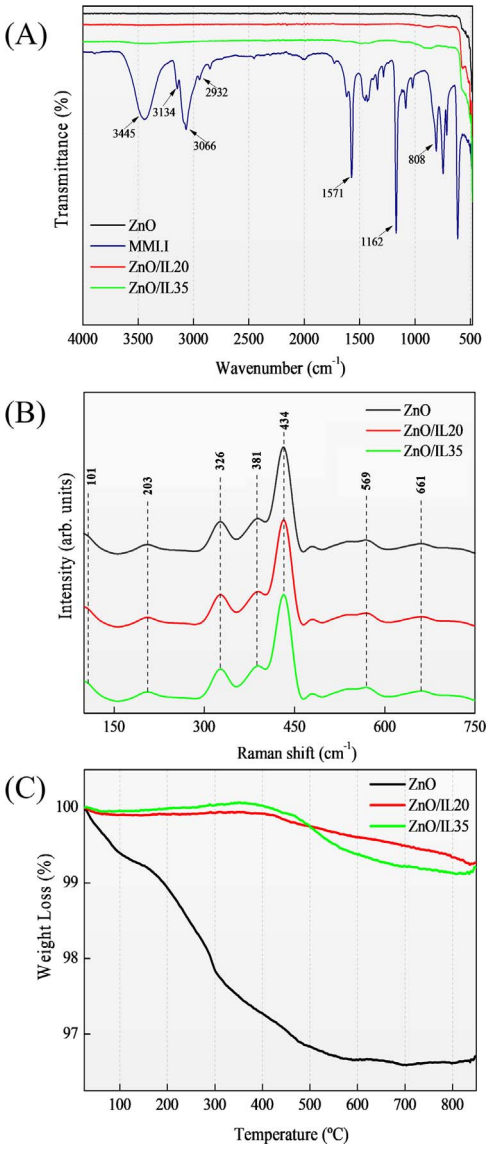

Fig. 2. ATR-FTIR spectra of ZnO, MMI.I IL, ZnO/IL20 and ZnO/IL35 (A), Raman spectra of ZnO, ZnO/IL20, and ZnO/IL35 (B) and, TG analysis of ZnO, ZnO/IL20, and ZnO/IL35 (C).

to the metal oxide stretching vibration, which is belonging to ZnO metal group. The MMI.I spectra show bands in the range of 2800–3200 cm^{-1} corresponding to CHx stretching region of the pure ILs [26]. The broadband at 3445 cm^{-1} is attributed to O-H binding of water from the air due to the MMI.I IL is very hygroscopic. The bands at 808 cm^{-1}, 1162 cm^{-1} and 1571 cm^{-1} are attributed to C-H of aromatic, –N–CH_2 and –N–CH_3 and, C=N stretching, respectively [27,28]. The bands in the range of 480–630 cm^{-1} refers to [I⁻] vibrations. The ZnO/IL samples have the same spectra profile as pure ZnO particles, but it can be seen that there is an increase in band intensity in the range of 480–585 cm^{-1} indicating that Zn-I binding may be occurring.

Raman spectroscopy was carried out to analyze any changes in the lattice vibrations of the ZnO nanostructure upon addition of IL. Fig. 2(B) displays the Raman spectra of ZnO and ZnO sensitized with IL. Wurtzite ZnO presents optical phonons at the Γ point of the Brillouin zone corresponding to the irreducible representation, Γopt = A_1 + E_1 + $2E_2$ + $2B_1$. The modes A_1 and E_1 are split into transverse (TO) and longitudinal optical (LO) phonons, while the E_2 modes are non-polar. The A_1 and E_1 modes are Raman and infrared active, the E_2 modes are only Raman active, and the B_1 modes are Raman and infrared inactive [29]. The zone center optical mode frequencies lie between about 100 cm^{-1} and 600 cm^{-1}. The group E_1 (LO), A_1 (LO), and B_1 (high) modes occurs in the highest frequency range, 550 cm^{-1} to 600 cm^{-1}. The groups E_2 (high), E_1 (TO), and A_1 (TO) appear between 370 cm^{-1} and 440 cm^{-1}. The E_2 (low) and the B_1 (low) modes appear in the frequencies 100 cm^{-1} and 250 cm^{-1}, respectively [30]. Fig. 2(B) shows a strong and dominant peak at 434 cm^{-1} for pure ZnO and ZnO/IL samples, attributed to the lattice vibration of oxygen atoms and mostly assigned to E_2 (high) phonon mode [31]. This peak at 101 cm^{-1} (E_2 low) are characteristic of scattering peaks of the Raman active dominant modes of wurtzite hexagonal ZnO, indicating the excellent quality of the crystal [29,32]. The peak at 381 cm^{-1} is attributed to the A_1 (TO) mode [30], while those at 203 and 326 cm^{-1} can be assigned to the acoustic phonon overtone and optical phonon overtone with the A_1 symmetry [32]. The Raman mode at 569 cm^{-1} corresponds to the E_1 (LO) mode of ZnO [29]. The peak at 661 cm^{-1} corresponds to additional vibrational modes associated with defects [33]. It is possible to observe that the addition of different amounts of ionic liquid does not change the lattice vibrations of the ZnO nanostructure.

Finally, TG investigation was performed to obtain information regarding decomposition temperatures and phase transformations. Fig. 2(C) shows the TGA curves of ZnO, ZnO/IL20, and ZnO/IL35. The TG curve of pure ZnO shows four weight loss stages. The first stage, in the temperature range 50–150 °C, could be due to the general desorption of water, low molecular weight solvents/gases, and other degradation products. The second and third steps, in the range 150–500 °C, showed a loss of 3.1% that could be attributed to the loss of adsorbed substances on the oxide surface. The fourth stage of mass loss, at T > 500 °C, could be related to the decomposition of hydrocarbonated products. However, the ZnO/IL20 and ZnO/IL35 samples exhibited a mass loss of approximately 0.2% and 0.1%, respectively, in the range 150–500 °C. These results demonstrate that the composites are more stable, suggesting that the IL acts as a thermal stabilizer.

Fig. 3 shows the FEG-SEM micrographs of the surface of the FTO, ZnO, and ZnO/IL samples.

Fig. 3(a) and (b) reveal that the FTO substrate has a dense homogeneous microstructure composed of spherical grains. Fig. 3(c) and (d) show that the surface of the ZnO deposited on the FTO substrate presents a micro flower-like morphology formed by nanopetals with a hierarchical structure. These ZnO flower structures present a porous surface that can be beneficial for applications such as advanced catalysts, gas sensors, and solar cells [34]. When the IL was added to the ZnO particles, no changes were observed in the micro flower-like morphology (Fig. 3(e)–(h)); however, the microstructures are observed to coalesce. In order to determine if the ionic liquid causes changes in the ZnO particle size, the particle size and thickness of the particles were calculated. Fig. 4 shows the histograms and the average values of particles and thickness are listed in Table 2.

The data in Table 2 show that the average values of particle size (I) and thickness (II) of pure ZnO were 2.65 and 0.036 μm, respectively. This particle size was similar to the reported values for the same structure, ~ 3 μm [34]. Upon the addition of IL, the average particle size decreased to 2.31 and 2.09 μm and the thickness to 0.029 and 0.026 μm for the ZnO/IL20 and ZnO/IL35 samples, respectively. This decrease in particle size upon the addition of ionic liquid has also been reported in the literature [35,36].

UV–vis spectroscopic measurements were carried out and the band gap energy (E_g, eV) of the samples calculated, in order to investigate the effect of the IL on the optical properties of ZnO (Fig. 5). The E_g of the samples was calculated by the Kubelka and Munk method [37], using the equation:

$$\alpha h\nu = A(h\nu - E_g)^n$$

where α is the linear absorption coefficient of the material, hν is the incident photon energy, A is a proportionality constant related to material, E_g is the band gap energy of the semiconductor, and n is a

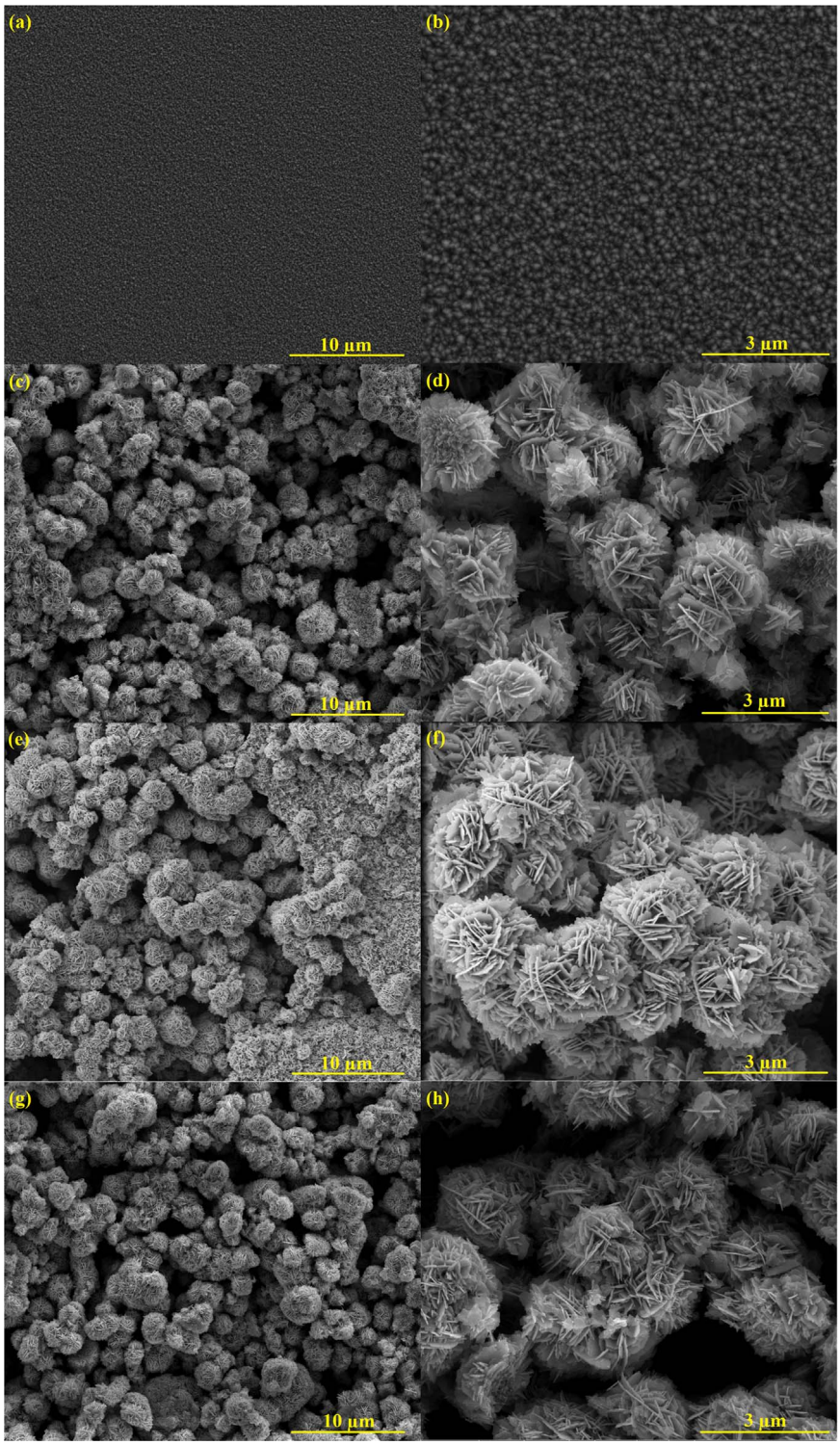

Fig. 3. FEG-SEM micrographs of FTO (a)–(b), ZnO (c)–(d), ZnO/IL20 (e)–(f), and ZnO/IL35 (g)–(h).

constant associated with different kinds of electronic transitions (n = 1/2 for a direct allowed transition; n = 2 for an indirect allowed transition). As previously reported, ZnO is an n-type direct band-gap semiconductor with n = 1/2 [38].

Fig. 5 shows the band gap values for ZnO, IL, ZnO/IL20, and ZnO/IL35 to be 3.16, 2.30, 3.14, and 3.09 eV, respectively. The E_g values found for ZnO and ZnO/IL samples were very similar, in agreement with a crystallographic profile similar to those indicated by XRD results. The band gap energy is described in the literature as direct electronic transitions from the maximum-energy states near or inside the valence band (VB) to minimum-energy states below or inside the conduction band (CB), in the Brillouin zone [39]. The theoretical band gap for ZnO powder is 3.3 eV [7,40]. Therefore, these results show that the ZnO particles synthesized in this work present defects, which introduce intermediate levels between the valence band and the conduction band.

Fig. 6 shows the PL spectra of ZnO, ZnO/IL20, and ZnO/IL35 using an excitation laser with λ = 350 nm at room temperature.

The profile of the PL emission band is typical of a multiphoton

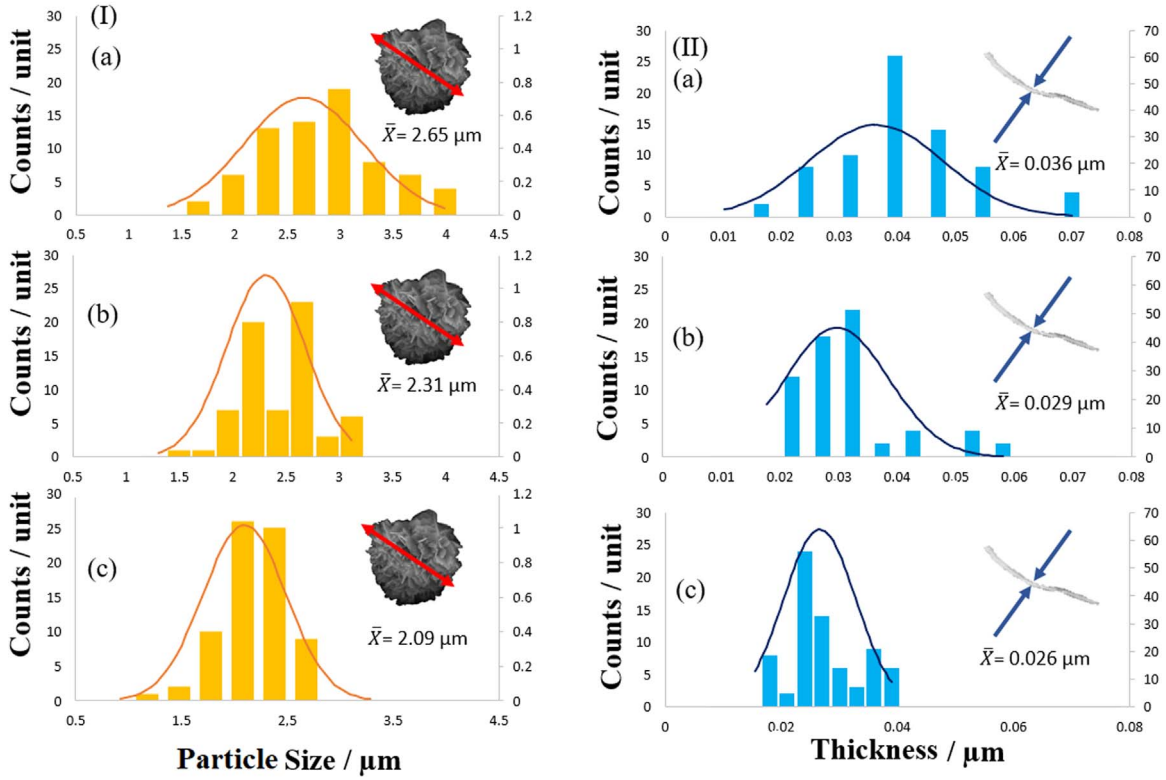

Fig. 4. Particle (I) and thickness (II) of ZnO (a), ZnO/IL20 (b), and ZnO/IL35 (c).

Table 2
Standard deviation (SD) of particle size and thickness for all samples.

Sample	Particle size (µm)	SD	Thickness (µm)	SD
ZnO	2.65	0.160	0.036	0.004
ZnO/IL20	2.31	0.128	0.029	0.002
ZnO/IL35	2.09	0.104	0.026	0.002

process, which involves different states within the band gap [41]. The PL spectrum of pure ZnO presents a broad band with the emission maximum centered at λ = 619.1 nm (2.0 eV). When the ZnO was doped with IL, the spectra had emission maxima centered at λ = 651.6 nm (1.90 eV) and λ = 653.0 nm (1.89 eV) for ZnO/IL20 and ZnO/IL35, respectively. To understand the PL properties and the contribution of each individual peak observed in the samples, we deconvolute these peaks using Voigt area function of the PickFit program (Fig. 6(b)–(d)). Pure ZnO spectrum has three components with energies centered at 2.20 (green), 1.97 (orange), and 1.77 eV (red) (Fig. 6(b)), corresponding to singled charged, doubly charged and excess oxygen defects [42]. Deconvolution analysis shows high percentage of contribution of the singled charged defects (green region) (42.3%), which could be related to the existence of shallow defects. These defects can be attributed to the recombination of isolated electrons in the vacancies of ionized oxygen (V_0) with photogenerated holes [43]. The spectra of ZnO/IL20 and ZnO/IL35 show the contribution of the three components located at the same energy values as pure ZnO (Fig. 8(c) and (d)); the deconvolution of these spectra show a shift of the maximum emission to the low energy region (red), accompanied by a decrease in the green contribution. Since singled charged oxygen vacancies are responsible for green emission, its reduction can be related with the decrease in the number of these vacancies type [44]. Thus, the addition of ionic liquid in the material decreases the number of oxygen vacancies and, as consequence, singled charged oxygen vacancies, but the number of doubly charged oxygen vacancies remains almost unchanged. It has already been reported in the literature that oxygen vacancies play a vital role in electrical conductivity of high surface area films, that is, a material with high concentration of surface defects has consequently poor electrical conductivity [45]. Therefore, it is expected that the ZnO/IL samples have best photocurrent density than ZnO, since the latter has high concentration of surface defects, which are mainly oxygen vacancies.

The pure and modified ZnO samples were taken in the form of pellets with diameter 5 mm, and then it was investigated how their PL emission spectra varied with temperature increase using different values in the range 32–298 K. Fig. 7 shows the PL spectra for the ZnO, ZnO/IL20, and ZnO/IL35 samples.

The PL spectra at different temperatures for ZnO, ZnO/IL20, and ZnO/IL35 show a decrease in intensity, red shift in emission energy, and broadening of the spectra with increasing temperature. At higher energy values (3.1–3.3 eV), emissions that could be attributed to localized bound-exciton (BX) recombination [46] were observed. As the temperature increased, BX recombination decreased rapidly. In the PL profile at 32 K for ZnO and ZnO/IL35 (Fig. 7(d)), we can differentiate ten PL peak positions. At 3.37 and 3.42 eV, free excitonic transitions due to the energy state n = 1($FX_A^{n=1}$) and the first excited energy state n = 2 ($FX_A^{n=2}$), respectively, are observed; these values are close to the predicted value of the A exciton [47]. The emission peak at 3.34 eV is assigned to the donor bound exciton, D_1X_A, and corresponds to A-excitons bound to a shallow donor. The other peaks observed on the lower energy side at 3.31, 3.24, and 3.17 eV are assigned as longitudinal optical (LO) replicas of $FX_A^{n=1}$; they occur due to free exciton transitions as well as bound exciton transitions. The peak corresponding to donor-acceptor-pair transitions (DAP) was located at 3.20 eV [48,49]. The PL profile of ZnO/IL35 reveals that the peak is broader than that of ZnO/IL20.

The current density–voltage curves both under illumination and in the dark were measured for ZnO and ZnO/IL films in acetonitrile solution with 10 mM LiI, 1 mM I_2, and 0.1 M $LiClO_4$, at a scan rate of 20

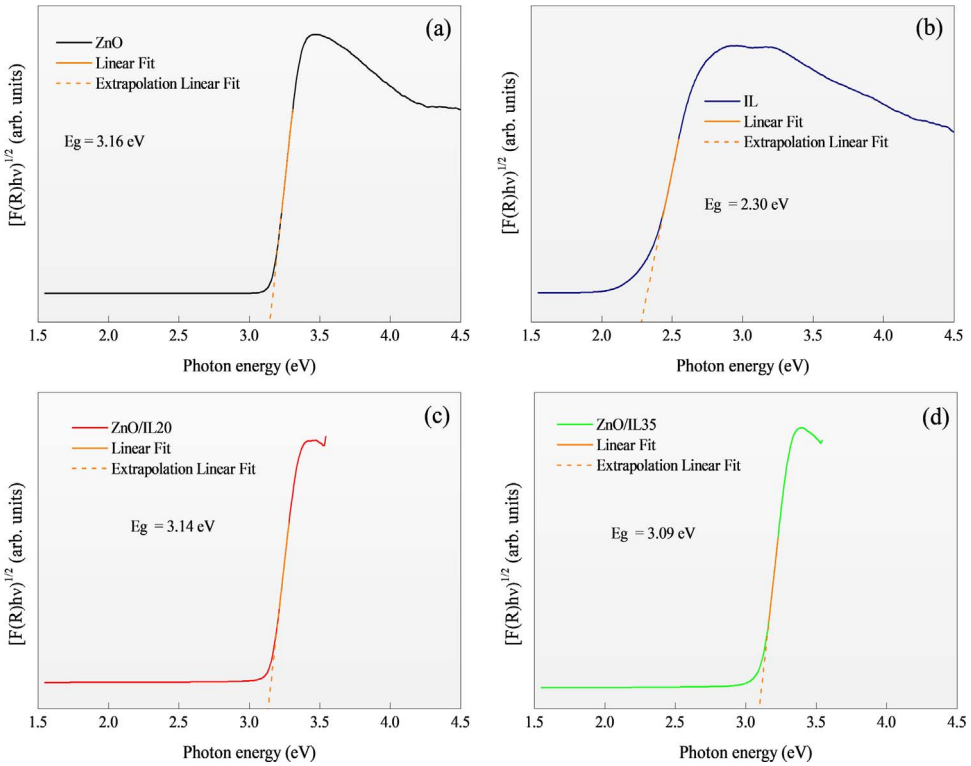

Fig. 5. Band gap energy of ZnO (a), MMI.I (b), ZnO/IL20 (c), and ZnO/IL35 (d).

mV s^{-1} (Fig. 8(A)).

As shown in Fig. 8(A), compared with the pristine ZnO film, the photocurrent density of ZnO/IL is significantly higher in both conditions. The photocurrent density in the dark increased from 0.07 mA cm^{-2} for pristine ZnO to 0.16 and 0.40 mA cm^{-2} for ZnO/IL20 and ZnO/IL35, respectively, at 1.08 V vs. Ag/AgCl. On the other hand, when the films are illuminated by a light source of 100 W of Xe, the photocurrent density increased from 0.05 mA cm^{-2} for pristine ZnO to 0.52 and 1.24 mA cm^{-2} for ZnO/IL20 and ZnO/IL35, respectively, at 1.08 V vs. Ag/AgCl. However, none of the curves show obvious changes in dark or under illumination. These results demonstrate that the MMI.I ionic liquid with a band gap energy of 2.30 eV has the potential to form a solar cell with high current density when combined with an appropriate n-type semiconductor, in this case ZnO.

To measure the photoresponse property, the FTO/ZnO/IL electrodes were tested at 1.08 V vs. Ag/AgCl in the range 0–400 s (Fig. 8(B)).

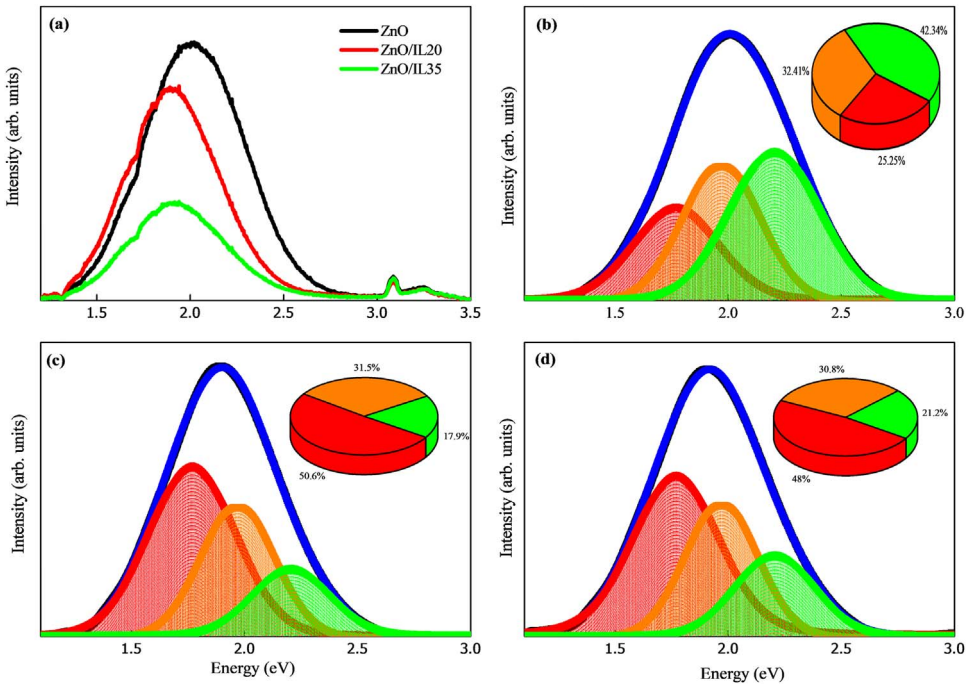

Fig. 6. Comparison of intensities of the photoluminescence curves for all samples (a) and the photoluminescence curves and deconvolution of the three peaks for ZnO (b), ZnO/IL20 (c), and ZnO/IL35 (d).

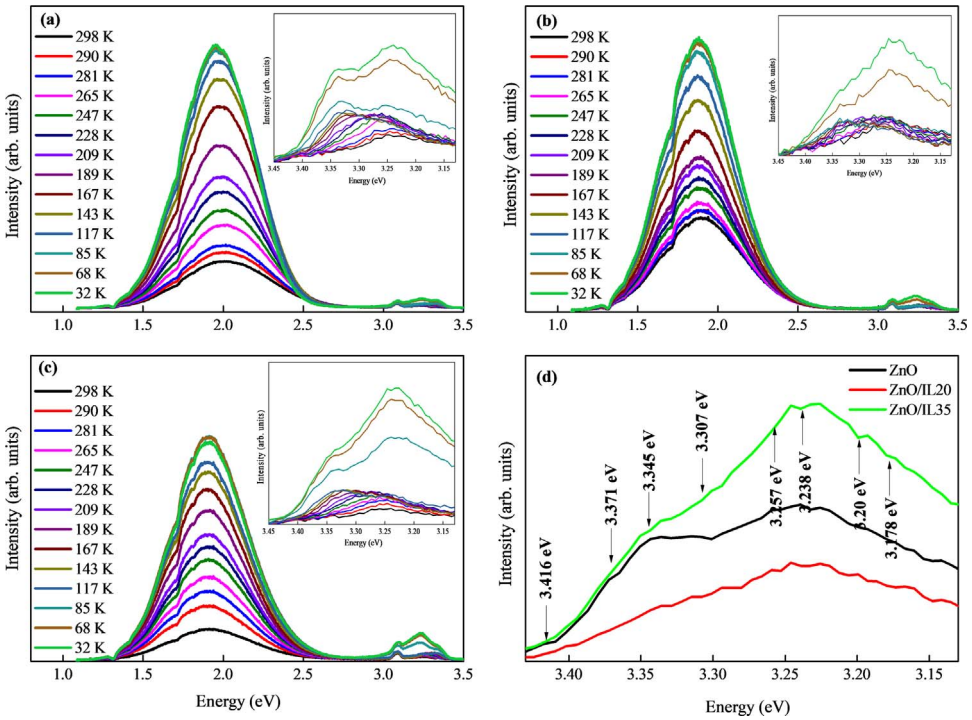

Fig. 7. Photoluminescence spectra at different temperatures for ZnO (a), ZnO/IL20 (b), ZnO/IL35 (c), and the PL profile of all samples in the region 3.37–3.13 eV at 32 K (d).

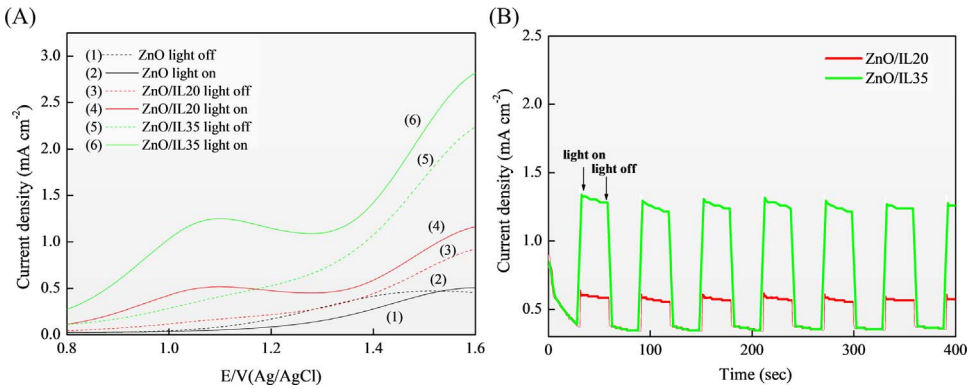

Fig. 8. J–V characteristics of ZnO and ZnO/IL samples, recorded in acetonitrile with 10 mM LiI, 1 mM I_2, and 0.1 M $LiClO_4$ in the dark (dashed lines) and under light (solid lines), and photoactivation currents measured at a potential of 1.08 V versus Ag/AgCl for FTO/ZnO/IL under Xe light illumination in acetonitrile with 10 mM LiI, 1 mM I_2, and 0.1 M $LiClO_4$.

As shown in Fig. 8(B), an atypical spike was observed in the photoresponse for both electrodes due to the transient effect in power excitation; the photocurrent then quickly returned to a steady state. This can be attributed to the fast recombination on the surface of the photoanode resulting from the limited hole-electron pair lifetime and poor minority carriers [50]. Due to the synergistic effect from doping and electrocatalyst loading, the FTO/ZnO/IL35 electrode performed better than the FTO/ZnO/IL20 electrode. The highest value of photocurrent obtained was 1.3 mA cm^{-2} for ZnO/IL35. This is higher than that obtained by Liu et al. [51] for a porous ZnO nanosheet with near-rectangular morphology at different annealing temperatures; the transient photocurrent response of the ITO/ZnO electrodes in on-off cycles, performed at a standard three-electrode cell, yielded a maximum photocurrent of 0.55 mA for the ZnO calcined at 500 °C, which was approximately 6 times greater than that of ZnO at 300 °C. This result was attributed to the more efficient separation of photogenerated electrons and holes.

Fig. 9 shows the energy band structure of ZnO/IL samples. The sensitization of ZnO particles by the MMI.I ionic liquid allows the photogenerated electrons (e^-) of IL to inject into the conduction band

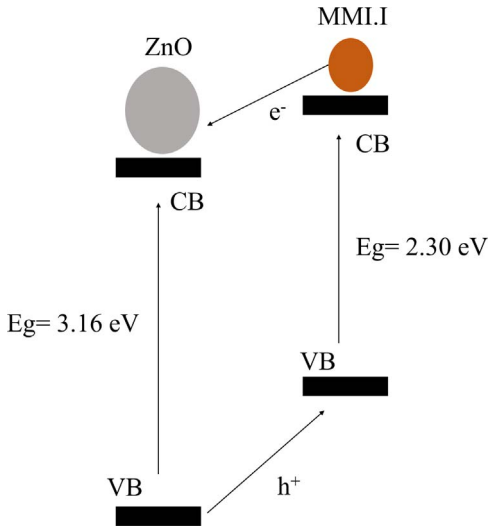

Fig. 9. Energy band structure of ZnO/IL samples.

(CB) of the oxide. The photogenerated holes (h^+) of oxide can also be easily transferred into the valence band (VB) of MMI.I. This process promotes charge separation.

The results showed that the addition of the 1.3-dimethylimidazolium iodide IL does not alter the crystal phase of ZnO; however, a subtle reduction in particle size was observed. This reduction can be attributed to hydrophilic nature and low surface tension of the ionic liquid, which may accelerate moderate interaction between the ZnO nuclei and I^-. Therefore the nucleation is increased in a faster rate to produce smaller size particles on the surface of the less coordinating and hydrophilic I^- anion. This interaction between the ZnO nuclei and the IL can lead to the formation of Zn-I binding, as shown in the ATR-FTIR spectrum, as well as the MMI.I IL may be acting as a dye, since it is constituted by an organic part, MMI^+. The performance of the MMI.I as a dye seems to be the most relevant hypothesis, since we have a 24-fold increase in the photocurrent density for the ZnO/IL35 sample. This result indicates that the ZnO particles were sensitized by the ionic liquid and, when radiation is present, the electrons of the IL are excited and it is able to transfer them to the ZnO conduction band. This good performance presented by the ZnO/IL 35 sample indicates that this is a promising material for photoanodes in solar cells.

4. Conclusions

ZnO particles synthesized by the microwave assisted hydrothermal method were sensitized with 1.3-dimethylimidazolium iodide ionic liquid and its photoluminescent and photoelectrochemical properties were investigated. X-ray diffraction analysis, field emission gun-scanning electron microscopy (FEG-SEM) and photoluminescence (PL) measurements confirmed the sensitization of the ZnO particles by the IL, indicating that the ionic liquid acts as a dye on the ZnO particles. Photoelectrochemical measurements revealed that the particles sensitized with 35% by mass of the MMI.I IL display potential for application as photoanodes in solar cells.

Acknowledgments

The support of this research by CNPq (159387/2015-9), FAPESP (2013/07296-2), and CAPES are gratefully acknowledged.

References

[1] P. Azadi, R. Malina, S.R.H. Barrett, M. Kraft, The evolution of the biofuel science, Renew. Sustain. Energy Rev. 76 (2017) 1479–1484, http://dx.doi.org/10.1016/j.rser.2016.11.181.
[2] H.-W. Wu, A review of recent development: transport and performance modeling of PEM fuel cells, Appl. Energy 165 (2016) 81–106, http://dx.doi.org/10.1016/j.apenergy.2015.12.075.
[3] J. Gong, K. Sumathy, Q. Qiao, Z. Zhou, Review on dye-sensitized solar cells (DSSCs): advanced techniques and research trends, Renew. Sustain. Energy Rev. 68 (2017) 234–246, http://dx.doi.org/10.1016/j.rser.2016.09.097.
[4] A. Chatzitakis, A. Papaderakis, N. Karanasios, J. Georgieva, E. Pavlidou, G. Litsardakis, I. Poulios, S. Sotiropoulos, Comparison of the photoelectrochemical performance of particulate and nanotube TiO2 photoanodes, Catal. Today 280 (2017) 14–20, http://dx.doi.org/10.1016/j.cattod.2016.07.017.
[5] N. Shahzada, D. Pugliese, V. Cauda, M.I. Shahzad, Z. Shah, M.A. Baig, E. Tresso, Comparative spectroscopic approach for the dye loading optimization of sheet-like ZnO photoanodes for dye-sensitized solar cells, J. Photochem. Photobiol. A 337 (2017) 192–197, http://dx.doi.org/10.1016/j.jphotochem.2017.01.011.
[6] S.S. Bhande, D.V. Shinde, K.K. Tehare, S.A. Patil, R.S. Mane, M. Naushad, Z.A. Alothman, K.N. Hui, S.H. Han, DSSCs synergic effect in thin metal oxide layer-functionalized SnO2 photoanodes, J. Photochem. Photobiol. A 295 (2014) 64–69, http://dx.doi.org/10.1016/j.jphotochem.2014.09.004.
[7] N. Roy, A. Chowdhury, A. Roy, Observation of negative differential resistance and electrical bi-stability in chemically synthesized ZnO nanorods, J. Appl. Phys. 115 (2014) 223502, http://dx.doi.org/10.1063/1.4882017.
[8] E.M. Kaidashev, M. Lorenz, H.V. Wenckstern, A. Rahm, H.-C. Semmelhack, K.-H. Han, G. Benndorf, C. Bundesmann, H. Hochmuth, M. Grundmann, High electron mobility of epitaxial ZnO thin films on c-plane sapphire grown by multistep pulsed-laser deposition, Appl. Phys. Lett. 82 (2003) 3901–3903, http://dx.doi.org/10.1063/1.1578694.
[9] K. Park, Q.F. Zhang, B.B. Garcia, X.Y. Zhou, Y.H. Jeong, G.Z. Cao, Effect of an ultrathin TiO2 layer coated on submicrometer-sized ZnO nanocrystallite aggregates by atomic layer deposition on the performance of dye-sensitized solar cells, Adv. Mater. 9 (2010) 2329–2332, http://dx.doi.org/10.1002/adma.200903219.
[10] J. Dupont, R.F. de Souza, P.A.Z. Suarez, Ionic liquid (molten salt) phase organometallic catalysis, Chem. Rev. 102 (2002) 3667–3691, http://dx.doi.org/10.1021/cr010338r.
[11] W. Xu, E.I. Cooper, C.A. Angell, Ionic liquids: ion mobilities, glass temperatures, and fragilities, J. Phys. Chem. B 107 (2003) 6170–6178, http://dx.doi.org/10.1021/jp0275894.
[12] W. Kunz, K. Häckl, The hype with ionic liquids as solvents, Chem. Phys. Lett. 661 (2016) 6–12, http://dx.doi.org/10.1016/j.cplett.2016.07.044.
[13] S. Artemenko, S. Haddad, V. Mazur, Azeotrope breaking potential of ionic liquids in separation processes, J. Mol. Liq. 235 (2017) 49–52, http://dx.doi.org/10.1016/j.molliq.2016.12.006.
[14] A. Eftekhari, Y. Liu, P. Chen, Different roles of ionic liquids in lithium batteries, J. Power Sources 334 (2016) 221–239, http://dx.doi.org/10.1016/j.jpowsour.2016.10.025.
[15] M. Díaz, A. Ortiz, I. Ortiz, Progress in the use of ionic liquids as electrolyte membranes in fuel cells, J. Membr. Sci. 469 (2014) 379–396, http://dx.doi.org/10.1016/j.memsci.2014.06.033.
[16] J. Li, J. Tang, J. Yuan, K. Zhang, Q. Shao, Y. Sun, L.-C. Qin, Interactions between graphene and ionic liquid electrolyte in supercapacitors, Electrochim. Acta 197 (2016) 84–91, http://dx.doi.org/10.1016/j.electacta.2016.03.036.
[17] S.M.M. Yusof, W.Z.N. Yahya, Binary ionic liquid electrolyte for dye-sensitized solar cells, Procedia Eng. 148 (2016) 100–105, http://dx.doi.org/10.1016/j.proeng.2016.06.453.
[18] Y. Cao, J. Zhang, Y. Bai, R. Li, S.M. Zakeeruddin, M. Grätzel, P. Wang, Dye-sensitized solar cells with solvent-free ionic liquid electrolytes, J. Phys. Chem. C 112 (2008) 13775–13781, http://dx.doi.org/10.1021/jp805027v.
[19] N.A.A. Latip, H.M. Ng, N. Farah, K. Ramesh, S. Ramesh, S. Ramesh, Novel development towards preparation of highly efficient ionic liquid based co-polymer electrolytes and its application in dye-sensitized solar cells, Org. Electron. 41 (2017) 33–41, http://dx.doi.org/10.1016/j.orgel.2016.11.040.
[20] K.-S. Kim, D. Demberelnyamba, B.-K. Shin, S.-H. Yeon, S. Choi, J.-H. Cha, H. Lee, C.-S. Lee, J.-J. Shim, Surface tension and viscosity of 1-butyl-3-methylimidazolium iodide and 1-butyl-3-methylimidazolium tetrafluoroborate, and solubility of lithium bromide + 1-butyl-3-methylimidazolium bromide in water, Korean J. Chem. Eng. 23 (2006) 113–116, http://dx.doi.org/10.1007/BF02705701.
[21] H.M. Rietveld, Line profiles of neutron powder-diffraction peaks for structure refinement, Acta Cryst. 22 (1967) 151–152, http://dx.doi.org/10.1107/S0365110×67000234.
[22] A.C. Larson, R.B. Von Dreele, General structure analysis system (GSAS), Los Alamos Natl. Lab. Rep. LAUR (2004) 86–748.
[23] B.H. Toby, EXPGUI, a graphical user interface for GSAS, J. Appl. Cryst. 34 (2001) 210–213, http://dx.doi.org/10.1107/S0021889801002242.
[24] D.M. Cunha, F.L. Souza, Facile synthetic route for producing one-dimensional zinc oxide nanoflowers and characterization of their optical properties, J. Alloy. Compd. 577 (2013) 158–164, http://dx.doi.org/10.1016/j.jallcom.2013.04.126.
[25] B. Lin, Z. Fu, Y. Jia, G. Liao, Defect photoluminescence of undoping ZnO films and its dependence on annealing conditions, J. Electrochem. Soc. 148 (2001) G110–G113, http://dx.doi.org/10.1149/1.1346616.
[26] S. Cha, M. Ao, W. Sung, B. Moon, B. Ahlström, Patrik Johansson, Y. Ouchid, D. Kim, Structures of ionic liquid–water mixtures investigated by IR and NMR spectroscopy, Phys. Chem. Chem. Phys. 16 (2014) 9591–9601, http://dx.doi.org/10.1039/C4CP00589A.
[27] J. Kiefer, J. Fries, A. Leipertz, Experimental vibrational study of imidazolium-based ionic Liquids: Raman and infrared spectra of 1-ethyl-3methylimidazolium bis(trifluoromethylsulfonyl) imide and 1-ethyl-3-methylimidazolium ethylsulfate, Appl. Spectrosc. 61 (2007) 1306–1311 ⟨http://dx.doi.org/0003-7028/07/6112-1306$2.00/0⟩.
[28] Q. Che, R. He, J. Yang, L. Feng, R.F. Savinell, Phosphoric acid doped high temperature proton exchange membranes based on sulfonated polyetheretherketone incorporated with ionic liquids, Electrochem. Commun. 12 (2010) 647–649, http://dx.doi.org/10.1016/j.elecom.2010.02.021.
[29] D.N. Montenegro, V. Hortelano, O. Martínez, M.C. Martínez-Tomas, V. Sallet, V. Munoz-Sanjosé, J. Jimenez, Non-radiative recombination centres in catalyst free ZnO nanorods grown by atmospheric-metal organic chemical vapour deposition, J. Phys. D: Appl. Phys. 46 (2013) 235302, http://dx.doi.org/10.1088/0022-3727/46/23/235302 (4pp).
[30] N. Roy, A. Chowdhury, T. Paul, A. Roy, Morphological, optical, and Raman characteristics of ZnO nanoflowers on ZnO-seeded Si substrates synthesized by chemical method, J. Nanosci. Nanotechnol. 16 (2016) 9738–9745, http://dx.doi.org/10.1166/jnn.2016.12355.
[31] R. Cusco, E. Alarcon-Llado, J. Ibanez, L. Artus, J. Jimenez, B. Wang, M.J. Callahan, Temperature dependence of Raman scattering in ZnO, Phys. Rev. B 75 (2007) 165202, http://dx.doi.org/10.1103/PhysRevB.75.165202.
[32] R. Zhang, P.-G. Yin, N. Wang, L. Guo, Photoluminescence and Raman scattering of ZnO nanorods, Solid State Sci. 11 (2009) 865–869, http://dx.doi.org/10.1016/j.solidstatesciences.2008.10.016.
[33] J. Sann, J. Stehr, A. Hofstaetter, D.M. Hoffmann, A. Neumann, M. Lerch, U. Haboek, A. Hoffmann, C. Thomsen, Zn interstitial related donors in ammonia-treated ZnO powders, Phys. Rev. B 76 (2007), http://dx.doi.org/10.1103/PhysRevB.76.195203 (195203-195203-6).
[34] Y. Sun, L. Wang, X. Yu, K. Chen, Facile synthesis of flower-like 3D ZnO superstructures via solution route, Cryst. Eng. Comm. 14 (2012) 3199–3204, http://dx.doi.org/10.1039/c2ce06335b.
[35] J. Shen, M. Shi, B. Yan, H. Ma, N. Li, M. Ye, One-pot hydrothermal synthesis of Ag-

reduced graphene oxide composite with ionic liquid, J. Mater. Chem. 21 (2011) 7795–7801, http://dx.doi.org/10.1039/c1jm10671f.
[36] J. Lu, J.-X. Yang, J. Wang, A. Lim, S. Wang, K.P. Loh, One-pot synthesis of fluorescent carbon nanoribbons, nanoparticles, and graphene by the exfoliation of graphite in ionic liquids, ACS Nano 3 (2009) 2367–2375, http://dx.doi.org/10.1021/nn900546b.
[37] P. Kubelka, F. Munk, Ein Beitrag zur Optik der Farbanstriche, Z. Techn. Phys. 12 (1931) 593–601.
[38] S. Yi, F. Zhao, X. Yue, D. Wang, Y. Lin, Enhanced solar light-driven photocatalytic activity of BiOBr–ZnO heterojunctions with effective separation and transfer properties of photo-generated chargers, New J. Chem. 39 (2015) 6659–6666, http://dx.doi.org/10.1039/c5nj00707k.
[39] M.L. Moreira, E.C. Paris, G.S. do Nascimento, V.M. Longo, J.R. Sambrano, V.R. Mastelaro, M.I.B. Bernardi, J. Andres, J.A. Varela, E. Longo, Structural and optical properties of CaTiO3 perovskite-based materials obtained by microwave-assisted hydrothermal synthesis: an experimental and theoretical insight, Acta Mater. 57 (2009) 5174–5185, http://dx.doi.org/10.1016/j.actamat.2009.07.019.
[40] Ü. Özgür, Y.I. Alivov, C. Liu, A. Teke, M.A. Reshchikov, S. Doğan, V. Avrutin, S.-J. Cho, H. Morkoç, A comprehensive review of ZnO materials and devices, J. Appl. Phys. 98 (2005) 041301–041404, http://dx.doi.org/10.1063/1.1992666.
[41] E.A.V. Ferri, T.M. Mazzo, V.M. Longo, E. Moraes, P.S. Pizani, M.S. Li, J.W.M. Espinosa, J.A. Varela, E. Longo, Very intense distinct blue and red photoluminescence emission in MgTiO3 thin films prepared by the polymeric precursor method: an experimental and theoretical approach, J. Phys. Chem. C 116 (2012) 15557–15567, http://dx.doi.org/10.1021/jp3021535.
[42] A. Samavati, Z. Samavati, A.F. Ismail, M.H.D. Othman, M.A. Rahman, I.S. Amiri, Effect of organic ligand-decorated ZnO nanoparticles as a cathode buffer layer on electricity conversion efficiency of an inverted solar cell, RSC Adv. 8 (2018) 1418–1426, http://dx.doi.org/10.1039/c7ra11902j.
[43] N. Roy, A. Roy, Growth and temperature dependent photoluminescence characteristics of ZnO tetrapods, Ceram. Int. 41 (2015) 4154–4160, http://dx.doi.org/10.1016/j.ceramint.2014.11.113.
[44] A. Kushwaha, M. Aslam, Defect induced high photocurrent in solution grown vertically aligned ZnO nanowire array films, J. Appl. Phys. 112 (2012) 054316, http://dx.doi.org/10.1063/1.4749808.
[45] A. Kushwaha, H. Tyagi, M. Aslam, Role of defect states in magnetic and electrical properties of ZnO nanowires, AIP Adv. 3 (2013) 042110, http://dx.doi.org/10.1063/1.4801937.
[46] L. Wang, N.C. Giles, Temperature dependence of the free-exciton transition energy in zinc oxide by photoluminescence excitation spectroscopy, J. Appl. Phys. 94 (2003) 973–978, http://dx.doi.org/10.1063/1.1586977.
[47] J. Lagois, Dielectric theory of interacting excitonic resonances, Phys. Rev. B 16 (1977) 1699–1705, http://dx.doi.org/10.1103/PhysRevB.16.1699.
[48] S.K. Tiwari, Defect related photoluminescence and EPR study of sintered polycrystalline ZnO, arXiv Prepr. arXiv 1202 (2012) 6335 〈https://arxiv.org/ftp/arxiv/papers/1202/1202.6335.pdf〉.
[49] A. Teke, Ü. Özgür, S. Doğan, X. Gu, H. Morkoç, Excitonic fine structure and recombination dynamics in single-crystalline ZnO, Phys. Rev. B 70 (2004), http://dx.doi.org/10.1103/PhysRevB.70.195207 (195207-195207-10).
[50] K. Sivula, F. Le Formal, M. Grätzel, Solar water splitting: progress using hematite (α-Fe2O3) photoelectrodes, ChemSusChem 4 (2011) 432–449, http://dx.doi.org/10.1002/cssc.201000416.
[51] D. Liu, Y. Lv, M. Zhang, Y. Liu, Y. Zhu, R. Zong, Y. Zhu, Defect-related photoluminescence and photocatalytic properties of porous ZnO nanosheets, J. Mater. Chem. A 2 (2014) 15377–15388, http://dx.doi.org/10.1039/c4ta02678k.